communications biology

A Nature Portfolio journal

Article

https://doi.org/10.1038/s42003-026-09577-z

The perforant pathway and CA3-Schaffer collateral afferents coordinate to regulate spatial learning

Fengwen Huang [1,2] ✉, Stephen Temitayo Bello[1,3], Siu Hin Lau [1] & Jufang He [1] ✉

The entorhinal-hippocampal system constitutes a pivotal neural circuit in the central nervous system. It is critically involved in processing spatial learning and memory. However, the specific neural interactions between entorhinal inputs and intra-hippocampal subcircuits that underlie spatial coding remain elusive. To address this gap, we integrated multimodal approaches including in vivo calcium imaging, dual-color optogenetic manipulation, chemogenetic intervention, electrophysiological recordings, immunohistochemistry, and Morris water maze (MWM) behavior to dissect how entorhinal-hippocampal afferents modulate hippocampal computations. Intriguingly, CA1-projecting CA3 neurons exhibited pronounced hyperactivity during early spatial learning, with activity gradually declining after sustained task performance. Chemogenetic inactivation of medial entorhinal-hippocampal afferents attenuated both neural responses of CA1-projecting CA3 neurons and the performance of spatial learning, hinting that medial entorhinal cortex (MEC) inputs to the hippocampus are essential for animals to execute spatial tasks precisely. By implementing dual-light theta-burst stimulation to co-activate ChrimsonR-expressing CA3-CA1 afferents and Chronos-expressing MEC-CA1 terminals, we observed robust heterosynaptic long-term potentiation in the dorsal CA1 region in vitro brain slice. This neuroplasticity was mediated synergistically by activating both NMDA receptors and voltage-gated calcium channels. Our findings establish that entorhinohippocampal afferents exert multilevel regulatory control over hippocampal function, thereby advancing mechanistic understanding of memory-related neurological pathologies.

Navigation capability is crucial for survival in complex environments, both for humans and animals. Within the central nervous system (CNS), the dorsal hippocampus (DHP) and the medial temporal lobe (MTL) are key regions responsible for integrating and processing spatial cognition related to navigable spaces[1–3]. The DHP comprises the dentate gyrus (DG), Ammon's horn components (CA1, CA2, and CA3), and the subiculum[4,5], while the entorhinal cortex (EC) serves as a major interface with the DHP in the MTL, facilitating the encoding and retrieval of navigation-related information[6,7]. This includes contributions from both the lateral (LEC) and medial (MEC) entorhinal cortices[8,9]. Recent studies have well documented the critical role of entorhinal–hippocampal afferents (perforant pathway, PP) in regulating hippocampal functions, showing that manipulation of the PP afferents can significantly disrupt hippocampal processes and their associated behavioral outcomes[10,11].

The CA3-derived Schaffer collaterals (CA3-SC afferents) to CA1 pyramidal neurons (CA1 PNs) in the DHP are one of the most studied circuitry models for exploring hippocampal functions under various experimental conditions, including exposure to external chemical, biological, and physical stimuli[12–15]. CA1 PNs receive substantial innervation from both CA3 area inputs (SC) and layer II/III inputs from the MEC (PP)[16,17]. Previous studies have established that neural interaction between MEC efferents and intrahippocampal circuits underpins key hippocampal functions, including behavioral timescale synaptic plasticity (BTSP) and adaptive behaviors[18–21]. Magee and colleagues demonstrated that entorhinal cortex-driven synaptic plasticity is required for hippocampal over-representation of reward sites. Combining optogenetic inhibition, physiological recordings, and multi-environment experiments, they showed that entorhinal cortex layer III provides an instructive signal shaping

[1]Department of Neuroscience, City University of Hong Kong, Hong Kong, Kowloon Tong, China. [2]Department of ophthalmology, Stanford University, Stanford, CA, USA. [3]Centre for Regenerative Medicine and Health, Hong Kong Institute of Science & Innovation, Chinese Academy of Sciences, Hong Kong, China. ✉e-mail: fwhuang2@stanford.edu; jufanghe@cityu.edu.hk

hippocampal activity to highlight behaviorally relevant environmental features[18,19]. Additionally, Losonczy's group used in vivo subcellular imaging of EC axons in hippocampal CA1 during virtual reality navigation to reveal that while MEC specializes in location-context coding and lateral EC (LEC) in goal-oriented signals, both subregions transmit redundant spatial information during reward-based tasks[20]. Furthermore, inhibitory projections from the entorhinal cortex to the hippocampus play a critical, albeit understudied, role in memory precision[21]. Despite these insights, how EC-CA1 inputs modulate neural activity in CA3-Schaffer collateral (CA3-SC) afferents during spatial learning and the mechanisms of neuroplasticity in the dorsal hippocampal formation remain largely unexplored.

While it is well documented that CA3-SC projections are critical for spatial information processing[11,22,23], longitudinal monitoring of the activity of this input during spatial learning has been poorly explored. To address this gap, we combined fiber photometry with the MWM to record the bulk activity of CA3-SC synapses during spatial learning. Synaptic plasticity in CA1 is known to correlate with spatial learning and memory[24,25]. However, traditional electrical stimulation is unable to specifically activate distinct neural inputs to CA1, such as those from the subiculum or prefrontal cortex[26,27]. To overcome this limitation, we employed a dual-opsin approach (ChrimsonR and Chronos) to selectively target CA3 and MEC neurons. This allowed us to examine how inputs from these regions influence CA1 neuroplasticity and to begin to uncover molecular mechanisms underlying this dual input. We believe this manipulation provides different insights into hippocampal–entorhinal circuit function. Together, these results may help us better understand how MEC inputs modulate hippocampal functions both at the level of neuroplasticity (via dual optogenetics) and at the behavioral level (spatial learning), and add a layer of understanding to hippocampal–entorhinal circuitry.

Results

Neural dynamics of CA1-projecting CA3 neurons during spatial learning

Although Schaffer collateral (SC) projections from CA3 neurons (CA3-SC afferents) in the dorsal hippocampus (DHP) are recognized as a critical circuit for navigation information processing[28,29], the dynamic patterns of their neural activity during spatial navigation tasks remain poorly characterized. To delineate the functional role of these afferents in hippocampal-dependent navigation, we integrated fiber photometry with MWM behavioral assays to monitor calcium (Ca^{2+}) dynamics in CA1-projecting CA3 neurons during spatial learning and memory consolidation (Fig. 1A).

We stereotaxically injected the retrograde Ca^{2+} indicator AAV/Retro-syn-jGCaMP7s into the CA1 region to label CA1-projecting SC axons originating from CA3 neurons, followed by optical fiber implantation targeting SC fibers originating from CA3 neurons of wild-type (WT) mice (Fig. 1B). After 4 weeks of viral expression, robust GCaMP7s fluorescence was observed in CA3-SC afferents within the DHP (Fig. 1C, D). Additionally, the axonal signal in CA3 appears stronger than the dendritic labeling. This can be explained by the dense bundles of SC fibers compared to the more diffusely distributed dendrites of CA3 pyramidal neurons. During 3 consecutive days of MWM training, mice exhibited pronounced hyperactivity during early spatial learning, with activity gradually declining after sustained task performance (Fig. 1E, blue). This resulting heightened activity in the CA3 area is thought to be crucial for encoding spatial information. Importantly, the insignificant changes in Ca^{2+} activity of CA1-projecting CA3 neurons across naïve and trained stages suggest that these CA3 neurons may encode stable, unitary spatial representations rather than dynamic associative information. Concurrently, escape latency progressively decreased from the naïve state (trial-1) to the well-trained phase (trial-10, Fig. 1E, red).

Quantitative analysis revealed no significant difference in Ca^{2+} signal amplitude between initial and final trials during the memory retention task (Fig. 1F–H; $\Delta F/F$: trial-1 2.33 ± 0.28% vs. trial-10 2.47 ± 0.28%, Student's t-test; $t(12) = -0.374$, $p = 0.715$), suggesting that these CA3 neurons may encode stable, unitary spatial representations rather than dynamic associative information. This aligns with earlier literature showing that CA3 plays a crucial role in maintaining stable spatial representations and pattern completion[30]. Additionally, our data reveal substantial heterogeneity in CA3 neural activity across animals, particularly beyond 5 s. We further found that the Ca^{2+} response in animals strongly correlates with swimming speed ($R^2 = 0.92$; Supplementary Fig. 1B). This is consistent with a previous study showing that CA3 neurons exhibit higher firing rates during faster locomotion[31]. Moreover, simultaneous plotting of velocity and neural activity could help elucidate their relationship more precisely in future studies on spatial learning. Control experiments in GFP-expressing mice showed no training-dependent fluorescent fluctuations (Fig. 1I–K and Supplementary Fig. 1A; $\Delta F/F$: trial-1 0.13 ± 0.11% vs. trial-10 −0.06 ± 0.15%, Student's t-test: $t(10) = 0.875$, $p = 0.402$), confirming that observed Ca^{2+} transients specifically reflect neural activity in GCaMP7s-labeled CA3-SC afferents. Taken together, these results suggest that CA1-projecting CA3 neurons exhibit dynamic activity patterns during spatial learning. While this may implicate CA3–CA1 connectivity in the process, we cannot exclude contributions from other inputs such as CA2 or EC-CA3 projections, and more specific targeting strategies will be needed to clarify the precise role of CA3-SC synapses. For instance, CA3-specific Cre lines (Grik4-Cre) combine the Cre-dependent retroAAV-GCaMP to precisely monitor the neural response in the CA3 area during spatial learning[32].

Activation of MEC neurons increases neural responses in CA1-projecting CA3 neurons

Coordinated interactions among hippocampal afferents are essential for spatial information processing, enabling dynamic regulation of synaptic connections and population coding[33,34]. Within this circuitry, CA1 pyramidal neurons (CA1 PNs) integrate inputs from two principal sources: Schaffer collateral (SC) projections from CA3 neurons and perforant pathway (PP) inputs originating in layer II/III of the medial entorhinal cortex (MEC), with MEC-derived navigation signals undergoing hippocampal refinement[35,36]. To dissect how PP inputs modulate CA3-SC fiber dynamics, we employed fiber photometry coupled with optogenetic interrogation in the DHP (Fig. 2A).

Retrograde AAV/Retro-syn-jGCaMP7s was stereotaxically delivered to CA1 for selective labeling of CA3-SC afferents, while AAV9-CaMKIIα-ChrimsonR-mCherry (control: AAV9-CaMKIIα-mCherry) was injected into MEC to target PP inputs (Fig. 2B). Following 4 weeks of viral expression, dual optical fibers were implanted in CA3 (recording) and MEC (stimulation), with an additional 2-week recovery period (Fig. 2C–E). In our experimental setup, three different patterns of light stimulations (single light pulse, single light burst, and single light theta burst stimulation) were utilized for activating the ChrimsonR-expressing PP inputs, which represent non-physiological and physiological stimulation protocol[34].

Mice were allowed to freely explore the soundproof chamber. When exploratory behavior ceased, we delivered 635 nm light stimulation (2 ms pulse width) at varying power levels to activate ChrimsonR-expressing MEC neurons while recording Ca^{2+} responses in GCaMP-expressing CA1-projecting CA3 neurons. We selected 50% of maximum light power (6.0 mW) for our experimental paradigm because this intensity consistently produced clear, unimodal Ca^{2+} responses across all subjects. Notably, even at maximum light power, we observed no abnormal behaviors or convulsive symptoms. Intriguingly, single-pulse activation of MEC inputs evoked significant Ca^{2+} transients in GCaMP7s-labeled CA3-SC fibers (2 ms pulse with 6.0 mW) compared to GFP controls (Fig. 2F–I; $\Delta F/F$: $GCaMP_{lp}$ 2.98 ± 0.37% vs. GFP_{lp} −0.01 ± 0.12%, Welch's t-test; $t(9.27) = 6.92$, $p < 0.001$), implying MEC inputs might directly modulate the activity of CA1-projecting CA3 neurons. Additionally, burst stimulation induced stronger responses (4 light pulses with 40 Hz) under the same power (Fig. 2J–M; $\Delta F/F$: $GCaMP_{lb}$ 24.14 ± 2.52% vs. GFP_{lb} −0.01 ± 0.14%, Welch's test, $t(7.1) = 11.92$, $p < 0.001$). Remarkably, TBS generated sustained Ca^{2+} plateaus in CA3-SC fibers, with response magnitudes showing protocol-dependent gradation (Fig. 2N–P; $\Delta F/F$: $GCaMP_{ltbs}$ 46.30 ± 6.05% vs. GFP_{ltbs} −0.03 ± 0.24%, Welch's test, $t(7.02) = 7.42$, $p < 0.001$;

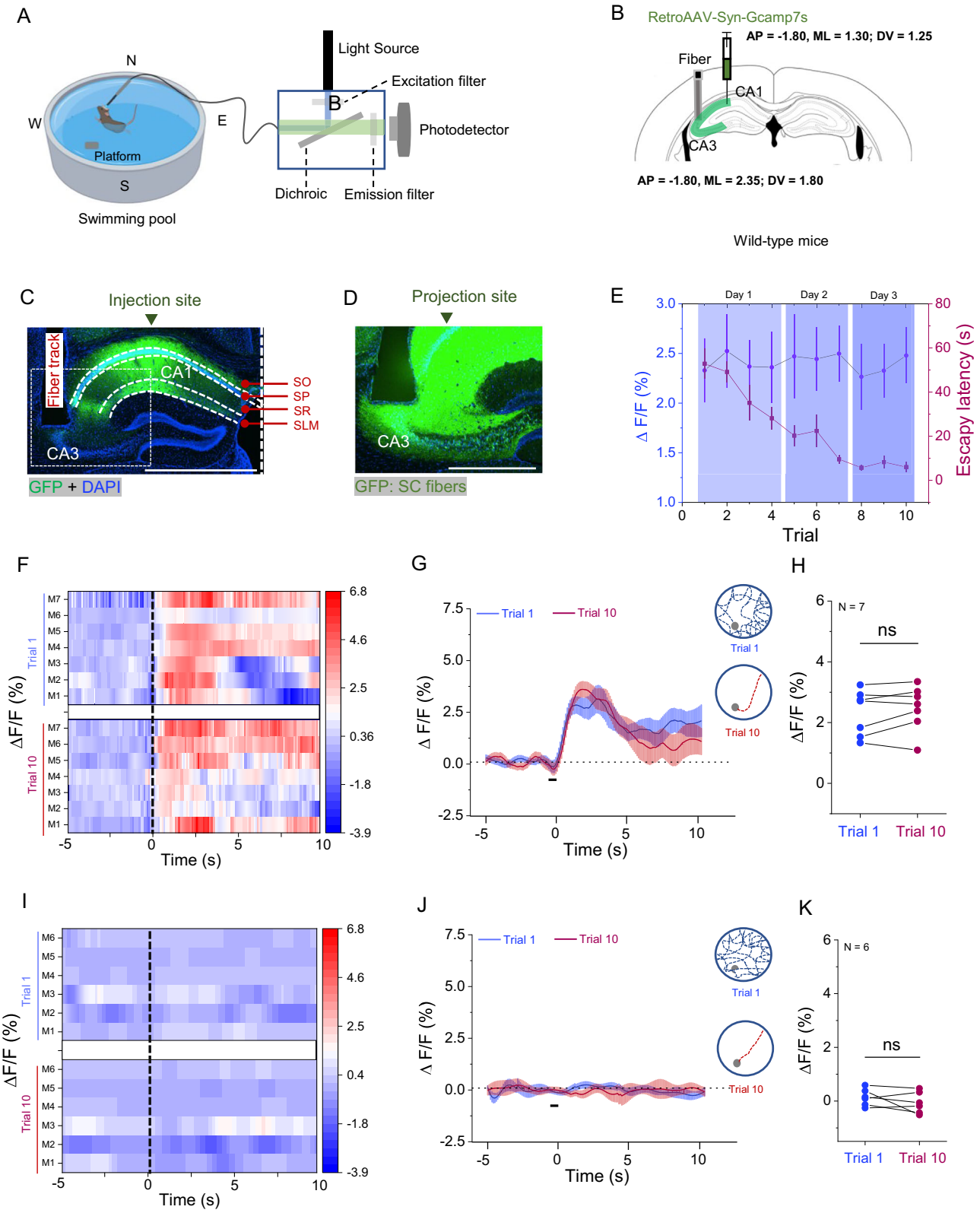

Supplementary Fig. 2A; Kruskal–Wallis test (non-parametric ANOVA) followed by Dunn's Post Hoc test with Bonferroni correction. $F(2,9.8) = 38.2$, $p < 0.001$; $GCaMP_{lp}$ vs. $GCaMP_{lb}$ $p = 0.002$; $GCaMP_{lp}$ vs. $GCaMP_{ltbs}$ $p < 0.001$; $GCaMP_{lb}$ vs. $GCaMP_{ltbs}$ $p = 0.001$). These results reveal that optogenetic activation of MEC neurons produces frequency-dependent increases in Ca^{2+} activity in CA1-projecting CA3 neurons.

Inhibition of MEC inputs attenuates the responses in CA1-projecting CA3 neurons

Our optogenetic findings demonstrate that activation of MEC inputs enhances CA3-SC neural activity. To determine whether MEC-CA1 neural integrity is required for maintaining these responses during spatial learning, we chemogenetically suppressed MEC-CA1 terminals during MWM

Fig. 1 | Neural dynamics of CA1-projecting CA3 neurons during spatial learning. **A** The schematic drawing shows the experimental setup for recording the neural activities during the Morris water maze (MWM) task. **B** AAV (250 nl AAV/Retrograde-syn-jGCaMP7s; 5.0E + 12 vg/ml) is injected into the CA1 the dorsal hippocampus (DHP). AAV injection (mm): AP = −1.80, ML = 1.30, DV = 1.25; Fiber implantation (mm); AP = −1.80, ML = 2.35, DV = 1.80. **C** Fluorescent image after adjusting the look-up table (LUT) showing the AAV expression in DHP and fiber track in CA3. Scale bar: 1000 μm. **D** Magnified image from Fig. 3C (dashed rectangle) shows optical fiber monitors the neuronal activities of CA3-SC afferents. Scale bar: 500 μm. **E** Double Y curves depict the escape latency and Ca^{2+} responses of GCaMP 7s-expressing mice during spatial learning. **F** The Ca^{2+} responses in trial-1 (upper) and trial-10 (lower) in GCaMP 7s-expressing mice. **G** The averaged Ca^{2+} responses in trial-1 (blue line) and trial-10 (red line). **H** Data were normally distributed (Shapiro–Wilk: Trial 1, $p = 0.538$; Trial 10, $p = 0.288$) with equal variances (Levene's test, $p = 0.934$). Statistical comparison of the averaged 5 s (after the 0 s) of Ca^{2+} responses in trial 1 (blue dots) and trial 10 (red dots) after mice are released into the swimming pool. **I** The Ca^{2+} responses in trial 1 (upper) and trial 10 (lower) in GFP-expressing mice. **J** The averaged Ca^{2+} responses in trial 1 (blue line) and trial 10 (red line) in control mice. **K** Data met normality (Shapiro–Wilk: Group A, $p = 0.879$; Group B, $p = 0.562$) and variance homogeneity (Levene's $p = 0.714$) assumptions. Statistical comparison of the averaged 5 s of Ca^{2+} responses in trial 1 (blue dots) and trial 10 (red dots) after control mice are released into the swimming pool. $^{*}p < 0.05$, $^{**}p < 0.01$, $^{***}p < 0.001$; ns not significant. Data are reported as mean ± SEM.

training (Fig. 3A). Retrograde AAV/Retro-syn-GCaMP7s was delivered to CA1 for monitoring the activity of CA1-projecting CA3 neurons, while AAV9-CaMKIIα-HM4DG(i)-mCherry (control: AAV9-CaMKIIα-mCherry) was injected into the MEC area (Fig. 3B). Following 6 weeks of viral expression, a drug cannula with integrated optical fibers was implanted above the CA1 area (Fig. 3C–F).

Our previous study has shown that local delivery of 300 nl (10 μM CNO) can effectively suppress the HM4D(Gi) expressing MEC-CA1 projections in the SLM layer and subsequently attenuate the animal's spatial learning[29]. We adopted the same manipulation in this experiment to inhibit HM4DG(i)-expressing MEC-CA1 terminals. This inhibition significantly reduced Ca^{2+} signals in CA1-projecting CA3 neurons throughout MWM training compared to mCherry controls (Fig. 3G). This suppression was evident both in the naïve (trial-1; Fig. 3I–K; $\Delta F/F$: HM4DG(i) 1.59 ± 0.25% vs. mCherry 2.55 ± 0.35%, Student's t-test, $t(12) = -3.20$, $p = 0.008$) and well-trained state (trial-10; Fig. 3L–N; $\Delta F/F$: HM4DG(i) 1.52 ± 0.26% vs. mCherry 2.31 ± 0.22%, Student's t-test, $t(12) = -3.02$, $p = 0.007$), suggesting that MEC inputs are critical modulators for innervating the function of CA1-projecting CA3 neurons. Consistent with these physiological changes, HM4DGi-expressing mice exhibited prolonged escape latencies and memory retention compared to controls (Fig. 3H; repeated measures ANOVA, group × trial interaction: $F(9,108) = 3.47$, $p < 0.001$; post-hoc at Trial 10: $t(12) = -2.42$, $p = 0.032$), indicating that MEC inputs are essential for animal to perform properly in the spatial task. Our results confirmed previous studies showing that MEC inputs support hippocampal-dependent spatial learning[6,20,37].

To functionally validate this interaction, we conducted in vitro field excitatory postsynaptic potentials (fEPSPs) recordings in DHP slices (Supplementary Fig. 3A). Electrical stimulation revealed that CNO application significantly decreased synaptic transmission in HM4DG(i)-expressing PP terminals compared to the mCherry-expressing controls (Supplementary Fig. 3B and C; HM4DG(i) 81.92 ± 4.12% vs. mCherry 101.26 ± 0.56%, Student's test, $t(7) = 7.64$, $p < 0.001$, $d = 2.70$). This chemogenetic suppression of MEC inputs to the hippocampus provides a mechanistic basis for the observed behavioral deficits and attenuated CA3 neural activity. While our chemogenetic inhibition of medial entorhinal cortex (MEC) inputs established their necessity for spatial learning and CA3-Schaffer collateral dynamics, this bulk manipulation approach cannot distinguish between specific pathways or cell types within the entorhinal–hippocampal network. This limitation precludes definitive conclusions about circuit-specific contributions. Nevertheless, these findings provide a critical foundation for future investigations employing pathway-specific interventions, for instance, inhibiting direct MEC-CA1 projections during distinct learning phases using retro-AAV delivery of Cre-dependent inhibitory opsins (e.g., Jaw 40) to MEC neurons projecting to dorsal CA1[38], coupled with closed-loop inhibition during specific behavioral epochs (acquisition vs. retrieval).

Co-activation of CA3–CA1 afferents and MEC-CA1 pathways induces heterosynaptic LTP

Although earlier studies have documented associative plasticity in CA1 using electrical stimulation[21,39,40], this approach lacks input specificity around the stimulation site. Dual-color optogenetic stimulation of presynaptic inputs provides a more precise way to investigate associative plasticity in the hippocampus. We therefore used ChrimsonR (red light-sensitive opsin) and Chronos (blue light-sensitive opsin) to selectively express in CA3–CA1 projections and MEC inputs, respectively, and studied associative plasticity in an optogenetic manner[41]. We developed a dual-color optogenetic strategy to probe heterosynaptic interactions. Using AAV9-CaMKIIα-ChrimsonR-mCherry (CA3-SC) and AAV9-CaMKIIα-Chronos-GFP (MEC-CA1) delivered to CA3 and MEC, respectively (Fig. 4A), we achieved pathway-specific labeling in DHP slices after 6 weeks of virus expression (Fig. 4B).

For the fEPSPs recording, we applied 473 and 635 nm light to each slice type and measured the responses (expressed either ChrimsonR in CA3–CA1 projections or Chronos in MEC-CA1 projections). We defined the crosstalk threshold as the 473 nm light power that evokes a response in ChrimsonR-expressing CA3–CA1 projections that is 10% of the maximum normalized fEPSP slope. We selected this 10% threshold because: (i) it would not induce significant fEPSPs slope in our system; (ii) this power of 473 nm light is sufficient to evoke robust responses in Chronos-expressing MEC-CA1 projections, enabling reliable induction of heterosynaptic-LTP (hetero-LTP) in the CA3-SC pathway during dual-color experiments. This approach ensures minimal non-specific activation while maintaining effective stimulation of the intended pathway (Supplementary Fig. 4A–D). The 635 nm stimulation selectively targeted ChrimsonR-SC afferents. For the dual-color optogenetic stimulation experiment, a 635 nm single light pulse with a one-minute interval was continuously delivered to activate the ChrimsonR-expressing CA3-SC synapses (Fig. 4D). A dual-wavelength theta-burst stimulation protocol (Fig. 4E; DL-TBS: 473 nm/40 Hz + 635 nm/40 Hz) enabled specific co-activation of Chronos-expressing MEC-CA1 projections and ChrimsonR-expressing CA3–CA1 projections in the CA1 area. Following a 20-min baseline recording of SC-evoked L-fEPSPs, DL-TBS induced robust hetero-LTP (Fig. 4F, red; SC + PP: 137.52 ± 3.72% vs. Control: 105.44 ± 2.32%, Welch's t-test, $t(10.2) = 6.11$, $p < 0.001$), compared to GFP controls (MEC inputs only expressing GFP; Fig. 4F, gray), suggesting that MEC inputs specifically facilitate the hetero-LTP formation in CA3-SC projections.

Furthermore, N-methyl-D-aspartate (NMDA) receptor | (NMDAR) plays a crucial role in E-TBS-mediated LTP formation[42,43]. Similarly, we observed that no significant hetero-LTP was formed in CA3-SC synapses after perfusing with NMDAR antagonist (100 μM APV; Supplementary Fig. 4E, F, red; Pre: 100.37 ± 0.39% vs. Post 103.35 ± 3.18%, Student test, $t(6) = 2.28$, $p = 0.062$, $d = 0.86$). Moreover, voltage-gated Ca^{2+} channels are involved in the formation of long-lasting Ca^{2+}-dependent plateau potential by the L-TBS of PP afferents[44,45]. We thus performed another set of experiments using the Ca^{2+} channel blocker (1 μM SNX) to inhibit the duration of Ca^{2+} influx in DHP. Intriguingly, hetero-LTP was significantly blocked by SNX (Supplementary Fig. 4E and G, gray; Pre: 100.99 ± 0.95% vs. Post 104.06 ± 1.75%, Student's test, $t(7) = 1.37$, $p = 0.212$, $d = 0.48$). These results indicate that light-evoked hetero-LTP shares common molecular channels with classic electrical stimulation-evoked LTP[42–45].

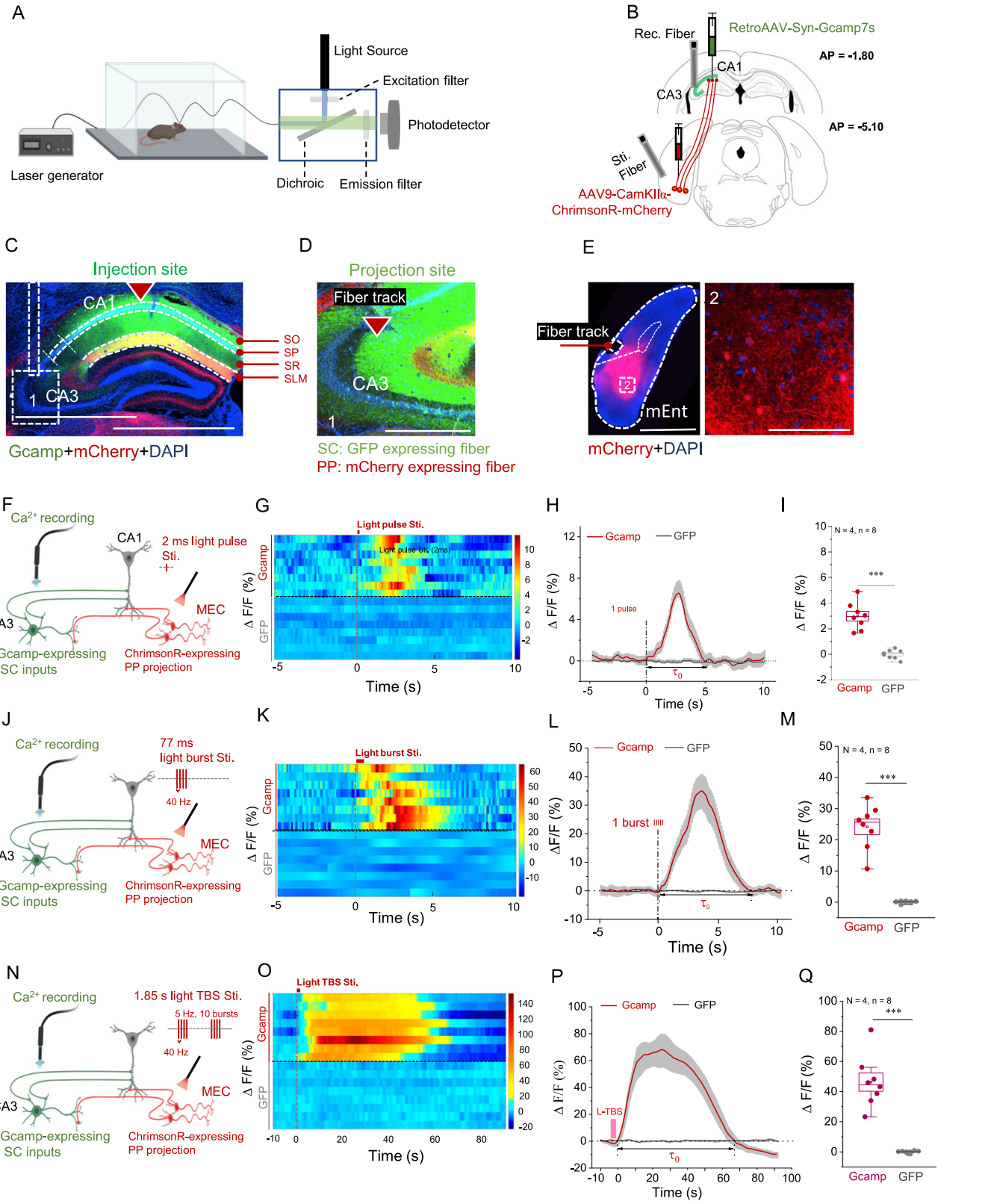

Optogenetic TBS fails to induce homosynaptic LTP in CA3–CA1 or MEC-CA1 pathways

Given the established role of hippocampal long-term potentiation (LTP) in spatial memory formation[46,47], we investigated whether pathway-specific optogenetic stimulation could induce homosynaptic plasticity. Dual viral strategies were employed: AAV9-CaMKIIα-ChrimsonR-mCherry-targeted CA3 neurons projecting to CA1 via Schaffer collaterals (CA3-SC), while AAV9-CaMKIIα-Chronos-GFP was delivered to medial entorhinal cortex (MEC) neurons forming perforant pathway (PP) inputs (Fig. 5A, B). Six weeks post-injection, robust opsin expression was confirmed in both pathways within DHP and MEC areas (Fig. 5C–F). While conventional electrical theta-burst stimulation (E-TBS; 100 Hz bursts at 5 Hz) reliably

Fig. 2 | Activation of MEC neurons increases neural responses in CA1-projecting CA3 neurons. **A** Schematic drawing shows the laser generator with fiber photometry. **B** Cartoon depicts the AAVs injection: 250 nl AAV/Retrograde-syn-jGCaMP7s in CA1 (5.0E + 12 vg/ml); 300 nl AAV9-CaMKIIα-ChrimsonR-mCherry for each of two sites in MEC (6.5E + 12 vg/ml); optical fibers implantation in DHP and MEC, respectively. AAV injection (mm) in CA1: AP = −1.80, ML = 1.30, DV = −1.25; In MEC: AP = −5.10, ML = 2.30, DV = −3.25/−2.75; Fiber implantation in CA3 (mm): AP = −1.80, ML = 2.30, DV = −1.80. In MEC: AP = −5.10, ML = 2.30, DV = −2.70. **C** Fluorescent image after adjusting the look-up table (LUT) showing the AAV expression in DHP and fiber track in CA3. Scale bar: 1000 μm. **D** Magnified image from Fig. 3C (dashed rectangle) shows an optical fiber monitors the neuronal activities of CA3-SC afferents. Scale bar: 500 μm. **E** AAV expression and optical fiber track in MEC. Scale bar: 1000 μm (right). Magnified image shows the AAV expression in MEC (left, site 2 in the above figure). Scale bar: 100 μm. **F** Schematic drawing illustrates the entorhinal–hippocampal circuitry and single light stimulation. **G** The Ca^{2+} responses in GCaMP 7s-expressing mice (upper) and GFP-expressing mice (lower) before and after the light stimulation. **H** Averaged Ca^{2+} responses in GCaMP 7s-expressing group (red line) and GFP group (black line) before and after the light stimulation. **I** Data met normality assumptions (Shapiro–Wilk $p > 0.05$) but violated variance homogeneity (Levene's $p = 0.021$). Statistical comparison of the averaged 5 s (after 0 s) of Ca^{2+} responses in the GCaMP 7s-expressing group (red dots) and GFP group (gray dots) after mice are released into the swimming pool. **J** Schematic drawing illustrates the entorhinal–hippocampal circuitry and light burst stimulation. **K** The Ca^{2+} responses in GCaMP 7s-expressing mice (upper) and GFP-expressing mice (lower) before and after the light stimulation. **L** Averaged Ca^{2+} responses in GCaMP 7s-expressing group (red line) and GFP group (black line) before and after the light stimulation. **M** Data met normality assumptions (Shapiro–Wilk $p > 0.05$) but showed severe variance heterogeneity (Levene's $p < 0.001$). Statistical comparison of the averaged 5 s of Ca^{2+} responses GCaMP 7s-expressing group (red dots) and GFP group (gray dots) after mice are released into the swimming pool. **N** Schematic drawing illustrates the entorhinal–hippocampal circuitry and light-TBS stimulation. **O** The Ca^{2+} responses in GCaMP 7s-expressing mice (upper) and GFP-expressing mice (lower) before and after the light stimulation. **P** Averaged Ca^{2+} responses in GCaMP 7s-expressing group (red line) and GFP group (black line) before and after the light stimulation. **Q** Data met normality assumptions (Shapiro–Wilk $p > 0.05$) but showed severe variance heterogeneity (Levene's $p < 0.001$), requiring Welch's test. Statistical comparison of the averaged 5 s of Ca^{2+} responses GCaMP 7s-expressing group (red dots) and GFP group (gray dots) after mice are released into the swimming pool. $^{*}p < 0.05$, $^{**}p < 0.01$, $^{***}p < 0.001$; ns not significant. Data are reported as mean ± SEM.

induces LTP[46,47], we developed an optogenetic TBS protocol (L-TBS; 40 Hz bursts at 5 Hz; Fig. 5G and L) that is adapted to opsin activation kinetics. Input–output curves confirmed light-intensity-dependent enhancement of evoked fEPSPs (L-fEPSPs) in both pathways (Fig. 5H, I and M, N), confirming successful optogenetic activation of synaptic transmission.

Notably, 635 nm L-TBS applied to CA3-SC terminals failed to induce persistent potentiation (Fig. 5J and K; Pre: 99.82 ± 0.54% vs. Post 106.30 ± 4.73%, Mann–Whitney U Test, $U = 48.0$, $p = 0.305$). Similarly, 473 nm L-TBS in PP terminals showed no significant plasticity (Fig. 5O and P; paired T-test; Pre: 98.72 ± 0.85% vs. Post 99.84 ± 1.22%, Student's t-test, $t(14) = -0.97$, $p = 0.349$). These results demonstrate that optogenetic theta burst stimulation alone is insufficient to elicit homosynaptic LTP in either pathway.

CA1-projecting MEC neurons are involved in spatial learning

Above experiments verified that MEC inputs are essential for innervating the hippocampal function at behavioral and synaptic levels. We next interrogated how MEC-CA1 afferents directly participate in spatial learning. Retrograde AAV/Retro-syn-jGCaMP7s was delivered to dorsal CA1 for selective monitoring of CA1-projecting MEC neurons during MWM navigation (Fig. 6A, B).

CA1-projecting MEC neurons were mainly located in layer II/III of MEC (Fig. 6C, D) by 6 weeks of AAV expression, consistent with prior anatomical findings[37]. While the majority of MEC-CA1 projections originate from layer III, a subset of MEC layer II "island cells" has been shown to directly innervate CA1[48,49]. These neurons preferentially target CA1 interneurons that modulate the distal dendritic activity of pyramidal cells. Our observations align with these findings, supporting the existence of a minor but functional MECII-CA1 pathway. Strikingly, longitudinal calcium imaging across three training days showed a progressive increase in the activities of CA1-projecting MEC neurons (Fig. 6E, blue), suggesting that increased MEC input activity is associated with spatial learning. Moreover, the sustained activity pattern aligns with prior reports of persistent firing in MEC neurons, a mechanism proposed to support spatial encoding and maintenance[6,20,37]. Particularly, a higher $\Delta F/F$ value was observed in trial-10 (well-trained, Fig. 6F–H, red) compared to that in trial-1 (naïve state; Fig. 6F–H, blue; $\Delta F/F$: trial-1 5.95 ± 1.29% vs. trial-10 7.52 ± 1.49%, Student's t-test, $t(10) = -1.41$, $p = 0.038$). Besides, escape latency in well-trained mice was significantly smaller than that in naïve-state (Supplementary Fig. 5A; trial-1 50.8 ± 8.12 s vs. trial-10 6.33 ± 1.91%, Wilcoxon test, $Z = 2.20$, $p = 0.028$), implying a normal capability for spatial learning. Taken together, these results suggest that MEC-hippocampal connections are necessary for hippocampal-dependent spatial behavior.

Discussion

In this study, we observed that both CA1-projecting CA3 neurons and CA1-projecting MEC neurons are involved in spatial learning, but through different neural dynamic patterns. Inhibition of MEC inputs significantly attenuates both the neural activity of CA1-projecting CA3 neurons and spatial learning, whereas hyperactivity of CA3 neurons remains necessary for spatial learning during the early stage. Hetero-LTP can be induced by simultaneous L-TBS of MEC inputs and CA3-SC synapses in vitro, and this form of LTP is mediated by NMDARs and voltage-gated calcium channels, representing a cellular mechanism for spatial learning. Thus, we uncovered a neural circuitry mechanism for spatial learning involving the coordination between MEC inputs and CA3-SC afferents. While our in vitro DL-TBS experiments demonstrate MEC's role in facilitating Hetero-LTP at CA3-SC synapses, this does not establish in vivo relevance to spatial performance. Future studies that employ in vivo electrophysiology recording at CA3-SC synapses during MWM learning might strengthen this connection within current data constraints.

Although the hippocampus has been extensively studied as an essential hub in the navigation system[22,50–52], the role of extra-hippocampal afferents in modulating intra-hippocampal circuits requires further investigation. The CA3–CA1 projections (CA3-SC inputs) serve as a widely used model to evaluate hippocampal functions under various physiological and non-physiological conditions[23,53,54]. In the current study, we utilized a calcium sensor (GCaMP-expressing AAV) to monitor dynamic changes in neural activity of the SC fibers of the dorsal hippocampal region in wild-type mice. We found that Ca^{2+} responses in CA3-SC fibers are crucial for navigation learning, as demonstrated in the MWM paradigm. Interestingly, neural activity in CA3-SC fibers was engaged throughout spatial training, from naïve to well-trained trials, with initial hyperactivity that diminished as performance stabilized. This finding further supports the notion that CA3-SC inputs are essential for hippocampal-dependent behaviors. A recent study suggests that spatial representations in CA3 neurons emerge gradually[55], demonstrating stable dynamics from trial to trial and day to day, implying that CA3 neurons perform significant computations on spatial inputs and play a distinct role in spatial memory processing.

The EC provides dense neural projections to the hippocampus, including inputs from the LEC and MEC[56,57]. It is commonly believed that the MEC supplies spatial information to the hippocampus, while the LEC conveys non-spatial information[58,59]. This interplay implies that the EC-hippocampal circuitry shapes ongoing intra- and extra-hippocampal processing. Specifically, MEC-derived projections to the hippocampus directly influence CA1 PNs and can enhance or suppress hippocampal activity through various mechanisms[21,60,61]. For example, CA1 PNs receive both

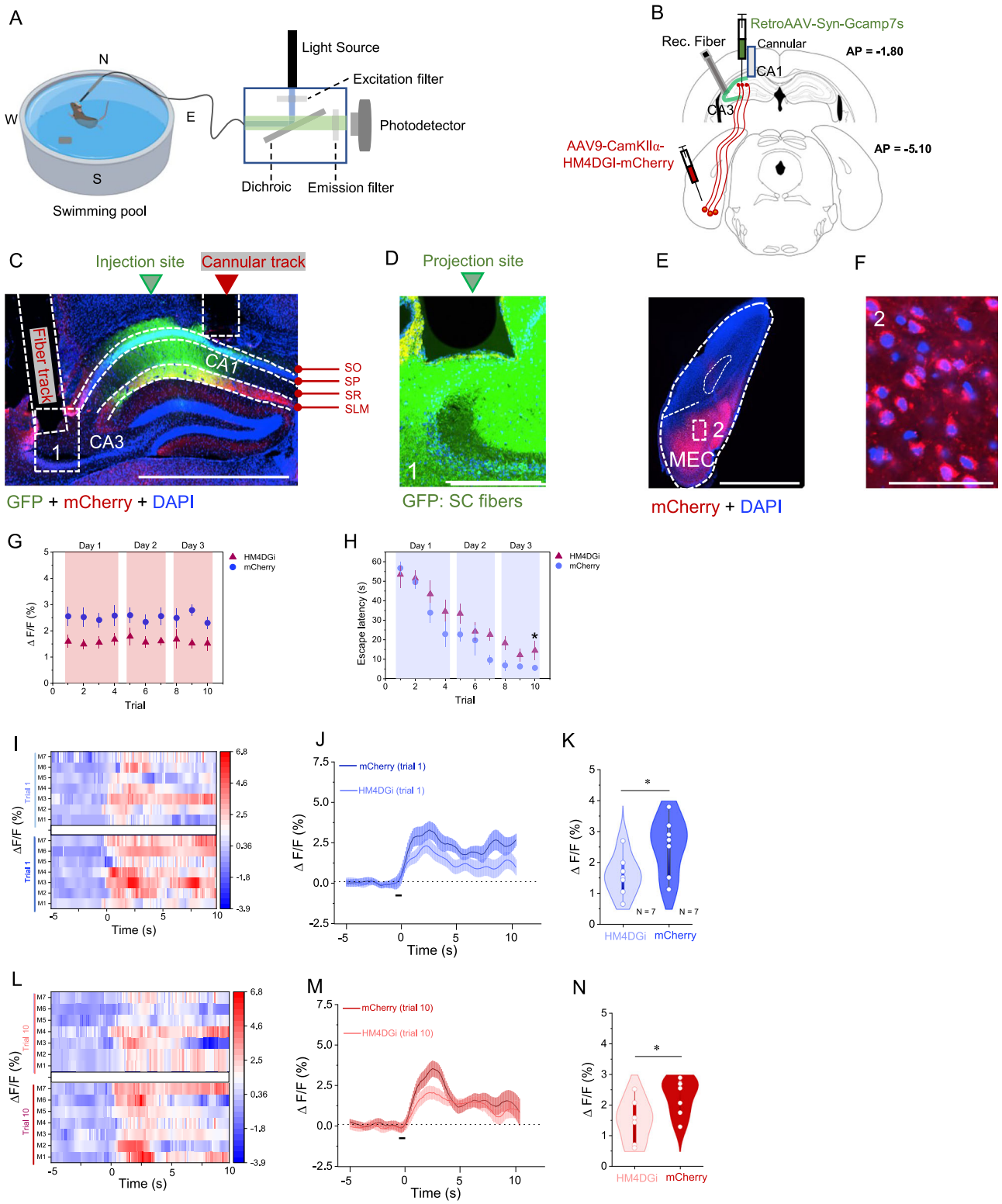

inhibitory and excitatory inputs from the MEC, which help regulate the neural state and behavioral outcomes. In this study, we demonstrated that the MEC provides robust excitatory projections to the CA1 region, effectively enhancing the neural activity of CA1-projecting SC synapses by stimulating the ChrimsonR-expressing PP inputs. This indicates that PP inputs from MEC neurons could interact directly with CA3-SC fibers. Notably, light theta burst stimulation of the PP inputs produced large-amplitude, long-duration Ca^{2+} responses at CA3-SC synapses, which may serve as a key neural mechanism for eliciting long-term neuroplasticity in CA1 PNs. Our results demonstrate a key functional interaction in this circuit, where MEC-derived sensory and spatial information modulates CA3 activity. Furthermore, MEC inputs are phase-locked to theta oscillations, which rhythmically gate CA3 activity to promote plasticity and memory encoding[56].

Indeed, inactivation of excitatory PP inputs both attenuated the neural activity of CA3-SC synapses and impaired spatial learning, further

Fig. 3 | Inhibition of MEC inputs attenuates the responses in CA1-projecting CA3 neurons. A The schematic drawing shows the experimental setup for inhibiting the PP inputs and recording the neural activities during the MWM task. **B** Cartoon depicts the AAVs injection; 200 nl AAV/Retrograde-syn-jGCaMP7s in CA1 (5.0E + 12 vg/ml); 300 nl AAV9-CaMKIIa-hM4D(Gi)-mCherry (5.0E + 12 vg/ml)/ AAV9-CaMKIIa-mCherry (5.0E + 12 vg/ml) for each of two sites in MEC; And cannular and optical fiber implantation in DHP, respectively. AAV injection (mm) in CA1: AP = −1.80, ML = 1.30, DV = 1.25; In MEC: AP = −5.10, ML = 2.30, DV = −3.25/−2.75; Cannular implantation in CA1 (mm): AP = −1.80, ML = 1.30, DV = −1.20. **C** AAVs expression in DHP, cannular in CA1, and fiber track in CA3. Scale bar: 1000 μm. **D** Magnified image shows that the optical fiber monitors the neuronal activities of CA3-SC afferents. Scale bar: 200 μm. **E** AAV expression and optical fiber track in MEC. Scale bar: 1000 μm. **F** Magnified image shows the AAV expression in MEC (left, site 2 in the above figure). Scale bar: 100 μm. **G** Ca^{2+} responses were markedly decreased in HM4DG(i)-expressing mice compared to the control mice (only expressing mCherry) during the spatial learning. **H** Escape latency was significantly impaired in HM4DG(i)-expressing mice compared to the control mice (only expressing mCherry). **I** The Ca^{2+} responses of trial-1 in HM4DG(i)-expressing mice (upper) and control mice (lower). **J** The averaged Ca^{2+} responses of trial-1in HM4DG(i)-expressing mice (wathet) and control mice (blue). **K** Data met normality (Shapiro–Wilk $p > 0.05$) and variance homogeneity (Levene's $p = 0.972$) assumption. Statistical comparison of the averaged 5 s of Ca^{2+} responses of trial-1 in HM4DG(i)-expressing group (wathet) and control (blue) after control mice are released into the swimming pool. **L** The Ca^{2+} responses of trial-10 in HM4DG(i)-expressing mice (upper) and control mice (lower). **M** The averaged Ca^{2+} responses of trial-10 in HM4DG(i)-expressing mice (pink) and control mice (red). **N** Data met normality (Shapiro–Wilk $p > 0.05$) and variance homogeneity (Levene's $p = 0.972$) assumption. Statistical comparison of the averaged 5 s of Ca^{2+} responses of trial-10 in HM4DG(i)-expressing group (pink) and control (red) after control mice are released into the swimming pool. $^{*}p < 0.05$, $^{**}p < 0.01$, $^{***}p < 0.001$; ns not significant. Data are reported as mean ± SEM.

demonstrating that the MEC-hippocampal circuitry is critical for processing and encoding spatial learning and memory. Additionally, the dynamics of neuroplasticity represent the neural mechanisms for integrating sensory, cognitive, and internal state information in the CNS[62–64]. Interestingly, high-frequency L-TBS of ChrimsonR-expressing CA3-SC synapses or Chronos-expressing MEC-CA1 afferents (PP inputs) failed to produce significant LTP compared to electrical theta burst stimulation (E-TBS). One reason for this discrepancy may involve differences in the neural or cellular mechanisms between light stimulation and electrical stimulation, warranting further investigation. However, robust and persistent heterosynaptic long-term potentiation was successfully induced in CA3-SC synapses through the co-activation of these two afferents in CA1 PNs, suggesting that PP inputs are essential for potentiating the neuroplasticity of CA3-SC synapses. Intriguingly, earlier studies demonstrated that co-activation of the Schaffer collateral (SC) and PP inputs triggered a prominent after-depolarizing potential (ADP)[33], which drove high-frequency action potential output in CA1 PNs, resulting in hetero-LTP.

Furthermore, we explored the cellular mechanisms mediating hetero-LTP in the dorsal hippocampus (DHP). Considering that N-methyl-D-aspartate receptors (NMDARs) are key mediators of LTP formation through high-frequency electrical stimulation in various brain regions, including the neocortex[44], hippocampus[65], and amygdala[66]. We thus utilized pharmacological methods to examine the role of NMDARs in DL-TBS-mediated hetero-LTP. Strikingly, the NMDAR antagonist APV significantly inhibited the potentiation of L-fEPSPs in CA3-SC synapses within the CA1 region, suggesting that DL-TBS-induced hetero-LTP is similar to E-TBS-mediated LTP. Moreover, the activation of voltage-gated calcium (Ca^{2+}) channels was also essential for NMDA-dependent LTP in the DHP[67]. Similarly, DL-TBS-induced hetero-LTP was dramatically blocked by the Ca^{2+} channel antagonist SNX-482. Taken together, our manipulation provides a sophisticated way for investigating the neural interaction and cooperation between two different pathways in the specific brain area, subsequently uncovering the mechanism of neuromodulator regulation in strengthening or weakening the synaptic plasticity, for instance, dopamine, serotonin, etc.

Finally, we elucidated the role of CA1-projecting MEC neurons in processing spatial learning and memory using the MWM paradigm. Our results showed that the neural activity of MEC inputs was significantly greater in well-trained mice compared to naïve mice. This finding implies that spatial-related memory information is likely encoded and processed in CA1-projecting MEC neurons, and subsequently processed in the DHP via direct or indirect pathways. Intriguingly, CA1-projecting MEC neurons remain hyperactive even after mice reach the platform. This sustained activity likely reflects ongoing spatial updating, memory consolidation, and environmental monitoring, aligning with the EC's role in maintaining a dynamic cognitive map beyond immediate navigation goals[68]. Furthermore, recent studies have comprehensively elucidated how efferent projections from the MEC to the hippocampus support spatial memory[6,20,37]. For instance, Malone et al. demonstrated that during learning in a new environment, MEC activity gradually becomes more spatially consistent and stabilizes. This increased consistency is thought to be driven by synaptic plasticity and a stable network of recurrent connectivity within the MEC. Additionally, Cholvin et al. employed two-photon calcium imaging in animals navigating through dissimilar virtual environments. The authors deciphered the relationship between the spatial properties of MEC inputs and the outputs of hippocampal pyramidal neurons in response to navigation through different environments, highlighting their potential role in spatial memory and recall. These findings suggest that the MEC plays a crucial role in forming and maintaining a cognitive map that supports spatial learning and navigation. Collectively, our experiments demonstrate that MEC inputs are crucial for the formation of heterosynaptic plasticity at CA3-SC synapses in area CA1 using a dual-color optical stimulation protocol. Complementing this, we further show that CA3-SC synaptic activity is functionally engaged during spatial memory acquisition. To directly test whether the heterosynaptic plasticity mechanism underlies the spatial behaviors, future studies could employ targeted, cell-specific interventions. For example, we could use activity-dependent viral expression to knock down the GluN1 subunit of NMDA receptors in CA1-projecting MEC neurons specifically during post-learning consolidation[69], and in vivo record the light-evoked fEPSPs at the CA3-SC synapses. This approach would test whether the plasticity is necessary for memory formation in vivo. Overall, this research provides different perspectives on how entorhinal–hippocampal afferents innervate intra-hippocampal circuitry at both behavioral and synaptic levels.

Methods

Animals

8–12 weeks old wild-type male mice (C57; RRID:IMSR_JAX:000664) were used in this study. In behavioral experiments, all male mice were housed in a 12 h light/dark cycle and were provided food and water ad libitum. All experimental procedures were approved by the Animal Subjects Ethics Sub-Committee of the City University of Hong Kong. We have complied with all relevant ethical regulations for animal use.

Viruses

Adeno-associated viruses (AAVs) were purchased from BrainVTA, Wuhan, China: AAV9-CaMKIIα-ChrimsonR-mCherry; AAV9-CaMKIIa-Chronos-GFP; AAV9-CaMKIIa-GFP; AAV9-CaMKIIa-hM4D(Gi)-mCherry; AAV9-CaMKIIa-mCherry; Addgene, Cambridge, MA, USA: AAV/Retrograde-syn-jGCaMP7s.

AAV injection

All adult mice were deeply anesthetized with pentobarbital sodium (50 mg/kg; Ceva Sante Animale Co., France). Then, anesthetized mice were head-fixed on a stereotaxic device, followed by a skin incision above the skull. The bregma and lambda were identified and balanced before AAV injection.

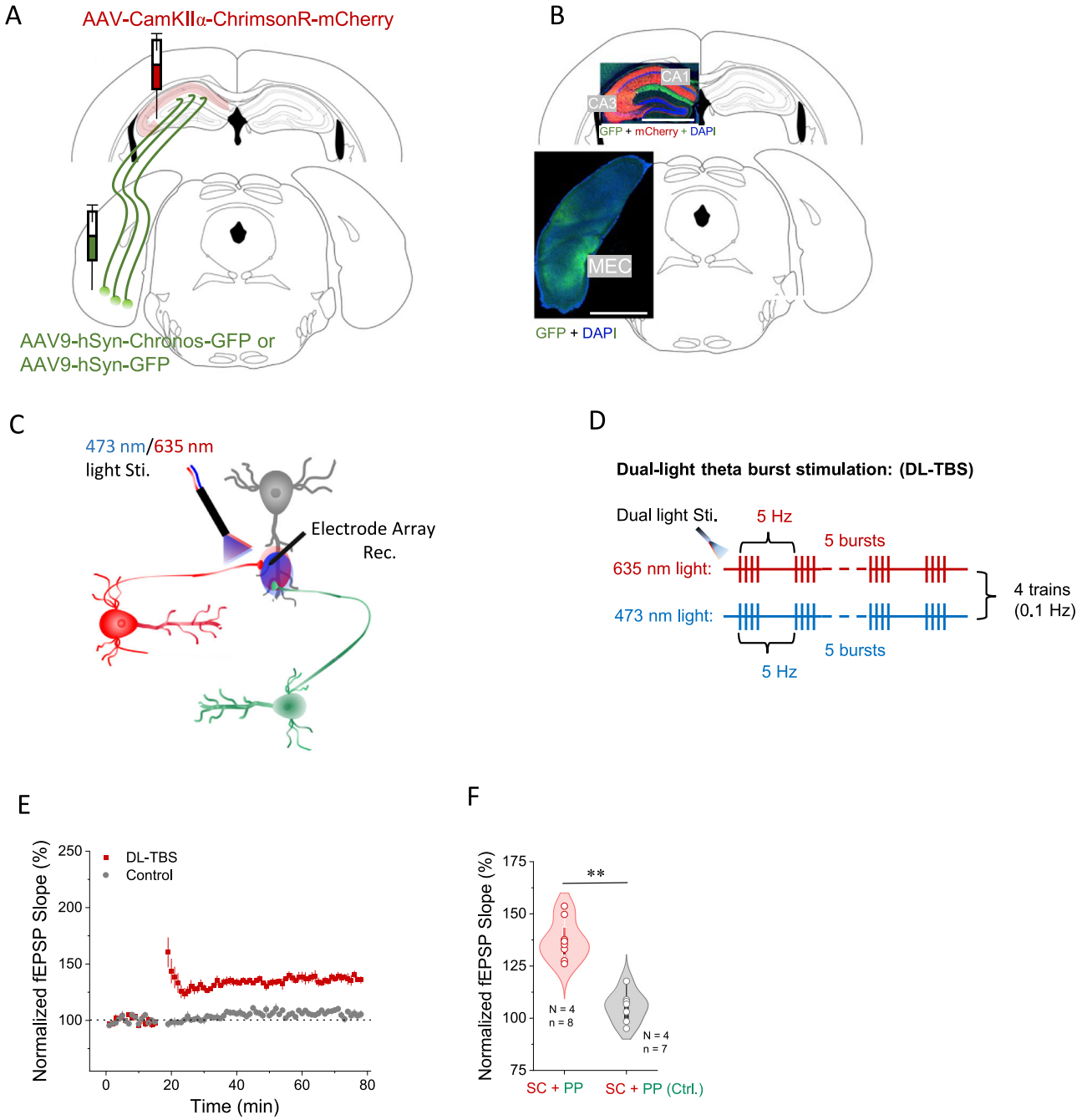

Fig. 4 | Co-activation of CA3-CA1 and MEC-CA1 pathways induces heterosynaptic LTP. A The schematic drawing shows the AAVs injection (AAV9-CaMKIIα-ChrimsonR-mCherry in CA3, AAV9-CaMKIIα-Chronos-GFP/AAV9-CaMKIIα-GFP in MEC) for targeting the CA3-SC afferents and PP inputs in WT mice. The injection volumes of AAVs are the same as Fig. 3. **B** Upper: AAV expression (ChrimsonR-mCherry) in CA3 neurons and SC fibers, and AAV expression (Chronos-GFP) in MEC-CA1 terminals in DHP. Scale bar: 1000 μm; Bottom: AAV expression (Chronos-GFP) in MEC neurons. Scale bar: 1000 μm. AAV injection (mm) in CA1: AP = −1.80, ML = 1.30, DV = 1.25; In MEC: AP = −5.10, ML = 2.30, DV = −3.25/−2.75. **C** Cartoon illustrates the 473 and 635 nm light stimulation of ChrimsonR-expressing CA3-SC afferents and Chronos-expressing PP inputs in the DHP, respectively. And recording of 473 and 635 nm L-fEPSPs in DHP. **D** The protocol of dual-colol theta burst light stimulation (DL-TBS) for activating the CA3-SC afferents and PP inputs. **E** DL -TBS successfully induced a robust and persistent hetero-LTP in CA3-SC afferents compared to the control group (only GFP-expressing PP inputs). **F** Data met normality assumptions (Shapiro–Wilk $p > 0.05$) but violated variance homogeneity (Levene's $p < 0.001$). Statistic comparison of 635 nm L-fEPSPs before and after DL-TBS. $N = 4$ mice, $n = 8$ recordings in DL-TBS group; $N = 4$ mice, $n = 7$ recordings in control. $^{*}p < 0.05$, $^{**}p < 0.01$, $^{***}p < 0.001$; ns not significant. Data are reported as mean ± SEM.

Next, AAV was prepared in a tough quartz glass micropipette with a fine tip mounted on a nanoliter 2000/Micro4 system. Craniotomies were made over the target location of the mouse's brain. For the positional parameters of the unilateral CA1 area, AAV was injected at AP: −1.80 mm, ML: 1.30 mm, DV: 1.25 mm. For the bilateral MEC, AAV was injected at AP: −5.10 mm, ML: ±2.30 mm, DV: −3.25/−2.75 mm. The volume and titer of AAV were depicted in the corresponding figure legends. The microinjection rate of AAV was 30 nl/min. Once the injection was completed, the glass micropipette was held in the target region for an additional 5 min before being withdrawn. Then, the surgical wound was sealed with stitches, and erythromycin ointment was used to prevent bacterial infection during the recovery. Mice were placed on a heating pad until they regained consciousness. Finally, mice were immediately returned to the Laboratory Animal Research Unit for regular holding.

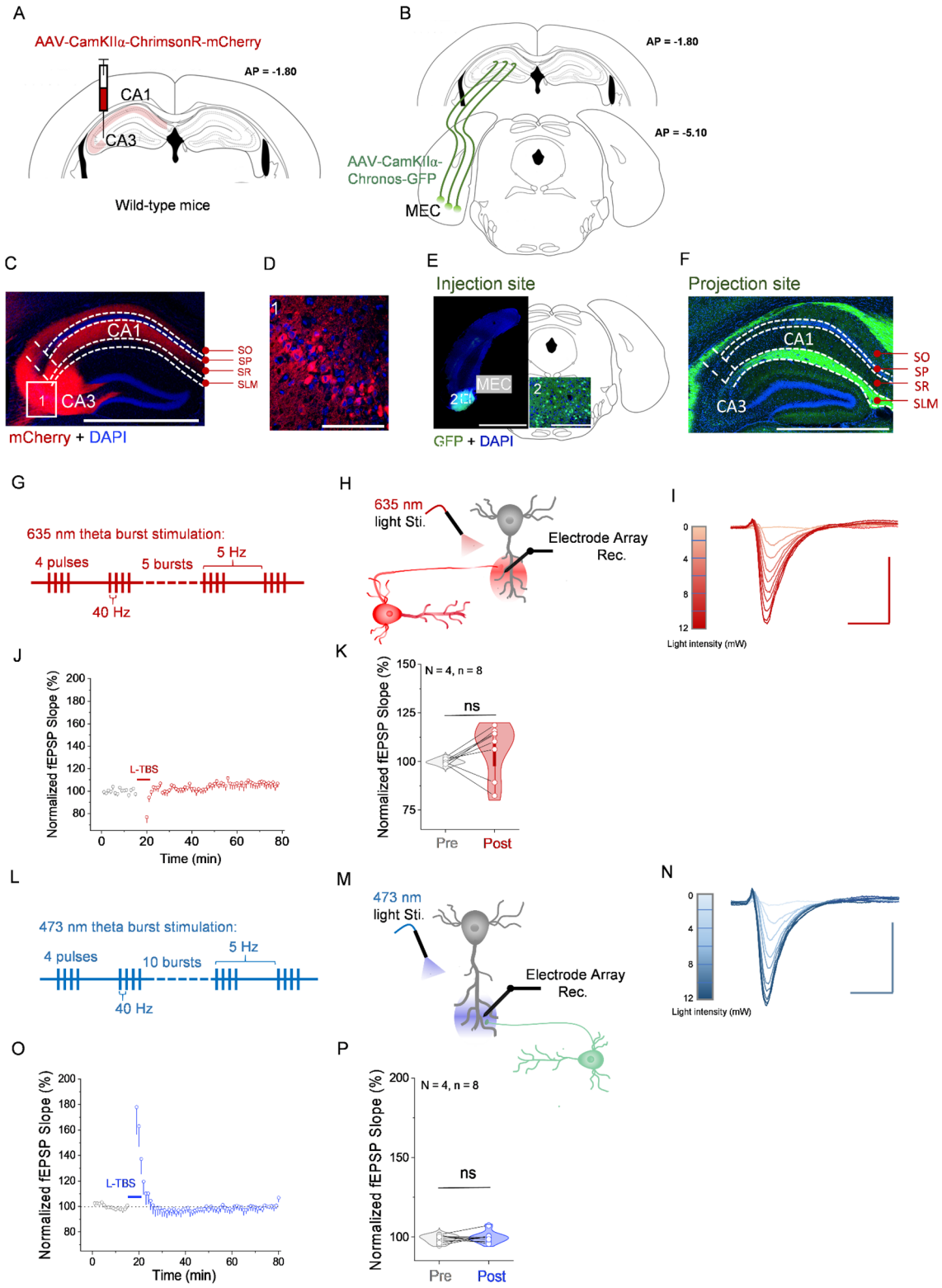

Figure 5.

Brian slice recording

In our experiment, mice were anesthetized with 1.4% gaseous isoflurane (Wellona Pharma, Surat, India). Then, mice were decapitated and brain was extracted and immersed in oxygenated (95% O_2–5% CO_2) ACSF solution: 124 NaCl, 3 KCl, 1.25 KH_2PO_4, 1.25 $MgSO_4$, 2 $CaCl_2$, 26 $NaHCO_3$ (in mM), and 10 glucose, pH ~ 7.4, which was prepared for the brain dissection, slicing, slice incubation and field EPSPs recording. The target brain region was placed onto the vibrating slicer (Leica VT1000S, Tokyo, Japan). Next, 300 μm-thick coronal slices were obtained and transferred to the incubation solution at 32 °C before performing the optogenetic and electrophysiological recording.

Fig. 5 | Optogenetic TBS fails to induce homosynaptic LTP in CA3–CA1 or MEC-CA1 pathways. A Schematic drawing shows the AAV injection (250 nl AAV9-CaMKIIα-ChrimsonR-mCherry: 7.5E + 12 vg/ml) into the CA1 area of the dorsal hippoca mpus (DHP). AAV injection (mm) in CA1: AP = −1.80, ML = 1.30, DV = 1.25. **B** Schematic drawing shows the AAV injection (300 nl AAV9-CaMKIIα-Chronos-GFP: 8.0E + 12 vg/ml) into each of three sites of the MEC area in WT mice. AAV injection (mm) in MEC: AP = −5.10, ML = 2.30, DV = −3.25/−2.75. **C** AAV expression in CA3 neurons and SC fibers. Scale bar: 1000 μm. **D** Magnified image shows that AAV is strongly infected in CA3 neurons. Scale bar: 200 μm. **E** AAV expression in the MEC area. Scale bar: 1000 μm. Magnified image shows that AAV is robustly expressed in MEC neurons. Scale bar: 100 μm. **F** AAV is robustly expressed in DHP (PP inputs). Scale bar: 1000 μm. **G** The protocol of 635 nm theta burst light stimulation (L-TBS) for activating the CA3-SC afferents in the CA1 area. **H** Cartoon illustrates the 635 nm light stimulation of ChrimsonR-expressing CA3-SC afferents and recording of fEPSPs in DHP. **I** A positive relation between light intensity and light-evoked fEPSPs; Scale bar: 0.5 mV/20 ms. **J** 635 nm L-TBS failed to elicit LTP at CA3-SC synapses. **K** Non-parametric analysis was required due to non-normality in post group (Shapiro–Wilk $p = 0.021$) and unequal variances (Levene's $p = 0.012$). Statistic comparison of 635 nm L-fEPSPs before and after 635 nm L-TBS. $N = 4$ mice, $n = 8$ recordings. **L** The protocol of 473 nm theta burst light stimulation (L-TBS) for activating the MEC inputs in the CA1 area. **M** Cartoon illustrates the 473 nm light stimulation of Chronos-expressing PP inputs and recording of fEPSPs in DHP. **N** A positive relation between light intensity and light-evoked fEPSPs; Scale bar: 0.5 mV/20 ms. **O** 473 nm L-TBS failed to elicit LTP at PP synapses. **P** Data met normality (Shapiro–Wilk $p > 0.05$) and variance homogeneity (Levene's $p = 0.663$) assumptions. Statistic comparison of 473 nm L-fEPSPs before and after L-TBS. $N = 4$ mice, $n = 8$ recordings. $^{*}p < 0.05$, $^{**}p < 0.01$, $^{***}p < 0.001$; ns not significant. Data are reported as mean ± SEM.

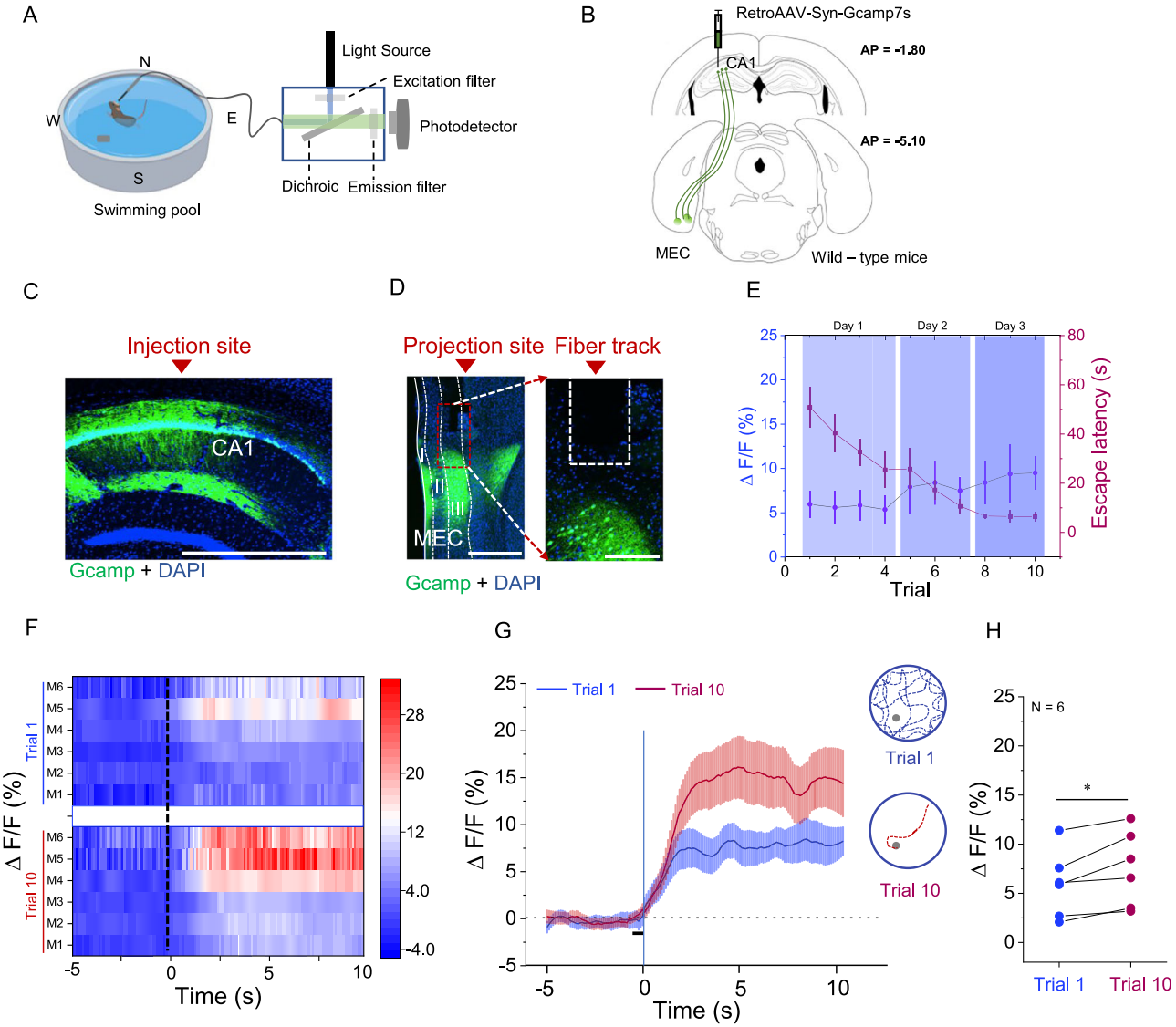

Fig. 6 | CA1-projecting MEC neurons mediate hippocampal spatial encoding. A The schematic drawing shows the experimental setup for recording the neural activities of PP inputs during the MWM task. **B** AAV (250 nl AAV/Retrograde-syn-jGCaMP7s; 5.0E + 12 vg/ml) is injected into the CA1 the dorsal hippocampus (DHP). AAV injection (mm) in CA1: AP = −1.80, ML = 1.30, DV = 1.25; Fiber implantation in MEC (mm): AP = −5.10, ML = 2.30, DV = −2.70. **C** AAV expression in the CA1 area. Scale bar: 1000 μm. **D** MEC neurons were retrogradely targeted by AAV (left), Scale bar: 500 μm; And the fiber track upon the layer II/III neurons in MEC (right). Scale bar: 200 μm. **E** Double Y curves depict the escape latency and Ca^{2+} of GCaMP 7s-expressing mice during spatial learning. **F** Ca^{2+} responses in trial-1 (upper) and trial-10 (lower) of GCaMP 7s-expressing mice during the spatial learning. **G** The averaged Ca^{2+} responses in trial-1 (blue line) and trial-10 (red line). **H** Data met normality (Shapiro–Wilk $p > 0.05$) and variance homogeneity (Levene's $p = 0.931$) assumptions. Statistical comparison of the averaged 5 s of Ca^{2+} responses in trial 1 (blue dots) and trial 10 (red dots) after mice are released into the swimming pool. $^{*}p < 0.05$, $^{**}p < 0.01$, $^{***}p < 0.001$; ns not significant. Data are reported as mean ± SEM.

An electrophysiological system (Alpha MED Sciences, Panasonic, Japan) combined with a light generator (Inper, Hangzhou, China) was adopted to record the electrical stimulus-evoked fEPSPs and light stimulus-evoked fEPSPs. Once the hippocampal slice was placed on the MED probes (2 × 8 electrodes), one of the electrodes was set as the stimulating electrode. For the light stimulation, a 2 ms light pulse was delivered to evoke a typical light-evoked field excitatory post-synaptic potential (L-fEPSP). Subsequently, an input/output (I/O) curve was performed to assess the induction of LTP. The stimulation intensity for the baseline synaptic response recording was set at 40% of the saturation level, and the stimulation intensity for theta burst stimulation (TBS) was adjusted to elicit 80% of the saturated intensity[66]. For the measurement of fEPSPs, we used the fEPSP slopes within the 10–90% range to quantify the responses, ensuring minimal contamination from population spikes. fEPSP slopes were normalized to the baseline mean, LTP amplitude was defined by the mean of fEPSPs recorded 50–60 min following induction[67]. Finally, the normalized fEPSP slope was computed by the MED Mobius software.

Fiber photometry recording and Morris water maze task

Fiber-photometry system (Doric Lenses) includes sinusoidally modulated light-emitting diodes (LEDs) at 473 nm (220 Hz) and 405 nm (330 Hz) as light sources to activate GCaMP and an isosbestic autofluorescence signal. Both lights were delivered to the implanted optical fiber in each mouse. The light intensity emitted from the fiber tip was 10 μW. Then, GCaMP and autofluorescence signals were gathered via the optical fiber and focused independently onto two separate photoreceivers (2151, Newport Corporation). An RZ5P acquisition system (Tucker-Davis Technologies; TDT), equipped with a real-time signal processor, controlled the LEDs and autonomously demodulated the fluorescence signal due to 473 and 405 nm excitations.

For the MWM task combined with GCaMP recording, adult male mice were subjected to the hidden platform to assess their swimming ability in a 60 cm radius swimming pool. During the 3-day training, mice were allowed to locate the hidden platform within 60 s, which was submerged in the water, and the light intensity was set bright enough for the video recording. Finally, photometry data were analyzed by an open-source software suite (pMAT). The fitted 405 nm signal was used to normalize the 473 nm signal. The calculation formula is as follows: $\Delta F/F_0$ = (473 nm signal-fitted 405 nm signal)/fitted 405 nm signal.

Chemogenetic manipulation

Cannulas were implanted into the bilateral area CA1 (AP: −1.70 mm, DV: −1.20 mm; ML: ±1.50 mm) in the C57 mice after the AAV injection. The surgical procedures were the same as those described above. Spatial memory tasks (MWM) and electrophysiological recordings were performed after AAV was expressed for 6 weeks. All animals in the experimental group (expressing HM4D(Gi)) and controls (expressing only mCherry) received local delivery of CNO into the bilateral area CA1 (10 μM, dissolved with 0.1% DMSO, Sigma-Aldrich; 300 nl for each site, 50 nl/min) via numerical control injector before conducting the behavioral task. For slice recording, 50 μM CNO was perfused into the recording solution (aCSF) during the process of electrical fEPSP recordings.

Statistics and reproducibility

All analyses were performed using GraphPad Prism v9.0, with validation of statistical assumptions. Data distributions were assessed for normality using the Shapiro–Wilk test (for sample sizes ≤ 50) or the Kolmogorov–Smirnov test (for sample sizes > 50) with a significance level of $\alpha = 0.05$. Homogeneity of variances was evaluated using Levene's test ($\alpha = 0.05$). All statistical tests were two-sided with $\alpha = 0.05$. Data are presented as mean ± standard error of the mean (SEM), statistical significance is denoted as $^{*}p < 0.05$, $^{**}p < 0.01$, and $^{***}p < 0.001$; ns indicates not significant ($p \geq 0.05$). The number of biological replicates (n) for each experiment is specified in the figure panels and result sections.

Data availability

Data are available upon reasonable request to the corresponding author. Numerical source data for all graphs in the manuscript can be seen in Supplementary Data File 1.

Received: 8 May 2025; Accepted: 12 January 2026;
Published online: 31 January 2026

References

1. Kunz, L. et al. A neural code for egocentric spatial maps in the human medial temporal lobe. *Neuron* **109**, 2781–2796.e10 (2021).
2. Chen, S., Cheng, N., Chen, X. & Wang, C. Integration and competition between space and time in the hippocampus. *Neuron* **112**, 3651–3664.e8 (2024).
3. Bonetti, L. et al. Spatiotemporal brain hierarchies of auditory memory recognition and predictive coding. *Nat. Commun.* **15**, 4313 (2024).
4. Imbrosci, B. et al. Subiculum as a generator of sharp wave-ripples in the rodent hippocampus. *Cell Rep.* **35**, 109021 (2021).
5. Zsido, R. G. et al. Ultra-high-field 7T MRI reveals changes in human medial temporal lobe volume in female adults during menstrual cycle. *Nat. Ment. Health* **1**, 761–771 (2023).
6. Malone, T. J. et al. A consistent map in the medial entorhinal cortex supports spatial memory. *Nat. Commun.* **15**, 1457 (2024).
7. Huang, F., Baset, A., Bello, S. T., Chen, X. & He, J. Cholecystokinin facilitates the formation of long-term heterosynaptic plasticity in the distal subiculum. *Commun. Biol.* **8**, 153 (2025).
8. Issa, J. B., Radvansky, B. A., Xuan, F. & Dombeck, D. A. Lateral entorhinal cortex subpopulations represent experiential epochs surrounding reward. *Nat. Neurosci.* **27**, 536–546 (2024).
9. Tacikowski, P., Kalender, G., Ciliberti, D. & Fried, I. Human hippocampal and entorhinal neurons encode the temporal structure of experience. *Nature* **635**, 160–167 (2024).
10. Chung, A. et al. Cognitive control persistently enhances hippocampal information processing. *Nature* **600**, 484–488 (2021).
11. Vanrobaeys, Y. et al. Mapping the spatial transcriptomic signature of the hippocampus during memory consolidation. *Nat. Commun.* **14**, 6100 (2023).
12. Tullis, J. E. et al. LTP induction by structural rather than enzymatic functions of CaMKII. *Nature* **621**, 146–153 (2023).
13. Chen, K. H. et al. Loss of the proton-activated chloride channel in neurons impairs AMPA receptor endocytosis and LTD via endosomal hyper-acidification. *Cell Rep.* **44**, 115302 (2025).
14. Zhang, X. et al. Modulating adult neurogenesis affects synaptic plasticity and cognitive functions in mouse models of Alzheimer's disease. *Stem Cell Rep.* **16**, 3005–3019 (2021).
15. Ravi, A. S. et al. Long-term potentiation reconstituted with an artificial TARP/PSD-95 complex. *Cell Rep.* **41**, 111483 (2022).
16. Lin, P. Y. et al. Neurexin-2: an inhibitory neurexin that restricts excitatory synapse formation in the hippocampus. *Sci. Adv.* **9**, eadd8856 (2023).
17. Sakalar, E., Klausberger, T. & Lasztóczi, B. Neurogliaform cells dynamically decouple neuronal synchrony between brain areas. *Science* **377**, 324–328 (2022).
18. Grienberger, C. & Magee, J. C. Entorhinal cortex directs learning-related changes in CA1 representations. *Nature* **611**, 554–562 (2022).
19. Bittner, K. C. et al. Conjunctive input processing drives feature selectivity in hippocampal CA1 neurons. *Nat. Neurosci.* **18**, 1133–1142 (2015).
20. Bowler, J. C. & Losonczy, A. Direct cortical inputs to hippocampal area CA1 transmit complementary signals for goal-directed navigation. *Neuron* **111**, 4071–4085 (2023).
21. Basu, J. et al. Gating of hippocampal activity, plasticity, and memory by entorhinal cortex long-range inhibition. *Science* **351**, aaa5694 (2016).

22. Nyberg, N., Duvelle, É, Barry, C. & Spiers, H. J. Spatial goal coding in the hippocampal formation. *Neuron* **110**, 394–422 (2022).
23. Sheintuch, L., Geva, N., Deitch, D., Rubin, A. & Ziv, Y. Organization of hippocampal CA3 into correlated cell assemblies supports a stable spatial code. *Cell Rep.* **42**, 112119 (2023).
24. Tsien, J. Z., Huerta, P. T. & Tonegawa, S. The essential role of hippocampal CA1 NMDA receptor–dependent synaptic plasticity in spatial memory. *Cell* **87**, 1327–1338 (1996).
25. Priestley, J. B., Bowler, J. C., Rolotti, S. V., Fusi, S. & Losonczy, A. Signatures of rapid plasticity in hippocampal CA1 representations during novel experiences. *Neuron* **110**, 1978–1992 (2022).
26. Sun, Y. et al. CA1-projecting subiculum neurons facilitate object–place learning. *Nat. Neurosci.* **22**, 1857–1870 (2019).
27. Malik, R., Li, Y., Schamiloglu, S. & Sohal, V. S. Top-down control of hippocampal signal-to-noise by prefrontal long-range inhibition. *Cell* **185**, 1602–1617 (2022).
28. Ayala, J. E. et al. mGluR5 positive allosteric modulators facilitate both hippocampal LTP and LTD and enhance spatial learning. *Neuropsychopharmacology* **34**, 2057–2071 (2009).
29. Su, J. et al. Entorhinohippocampal cholecystokinin modulates spatial learning by facilitating neuroplasticity of hippocampal CA3–CA1 synapses. *Cell Rep.* **42**, 113467 (2023).
30. Lee, I., Yoganarasimha, D., Rao, G. & Knierim, J. J. Comparison of population coherence of place cells in hippocampal subfields CA1 and CA3. *Nature* **430**, 456–459 (2004).
31. Ahmed, O. J. & Mehta, M. R. Running speed alters the frequency of hippocampal gamma oscillations. *J. Neurosci.* **32**, 7373–7383 (2012).
32. Madar, A. D., Jiang, A., Dong, C. & Sheffield, M. E. Synaptic plasticity rules driving representational shifting in the hippocampus. *Nat. Neurosci.* **28**, 1–13 (2025).
33. Takahashi, H. & Magee, J. C. Pathway interactions and synaptic plasticity in the dendritic tuft regions of CA1 pyramidal neurons. *Neuron* **62**, 102–111 (2009).
34. Ahmed, M. S. & Siegelbaum, S. A. Recruitment of N-Type Ca^{2+} channels during LTP enhances low release efficacy of hippocampal CA1 perforant path synapses. *Neuron* **63**, 372–385 (2009).
35. Tozzi, F. et al. Involvement of a lateral entorhinal cortex engram in episodic-like memory recall. *Cell Rep.* **43**, 114795 (2024).
36. Donohue, J. D. et al. Parahippocampal latrophilin-2 (ADGRL2) expression controls topographical presubiculum to entorhinal cortex circuit connectivity. *Cell Rep.* **37**, 110031 (2021).
37. Cholvin, T., Hainmueller, T. & Bartos, M. The hippocampus converts dynamic entorhinal inputs into stable spatial maps. *Neuron* **109**, 3135–3148 (2021).
38. Butola, T. et al. Hippocampus shapes entorhinal cortical output through a direct feedback circuit. *Nat. Neurosci.* **28**, 811–822 (2025).
39. Wöhrl, R., Von Haebler, D. & Heinemann, U. Low-frequency stimulation of the direct cortical input to area CA1 induces homosynaptic LTD and heterosynaptic LTP in the rat hippocampal–entorhinal cortex slice preparation. *Eur. J. Neurosci.* **25**, 251–258 (2007).
40. Masurkar, A. V. et al. Medial and lateral entorhinal cortex differentially excite deep versus superficial CA1 pyramidal neurons. *Cell Rep.* **18**, 148–160 (2017).
41. Huang, F., Bello, S. T., Baset, A., Chen, X. & He, J. Protocol for induction of heterosynaptic long-term potentiation in the mouse hippocampus via dual-opsin stimulation technique. *STAR Protoc.* **5**, 102860 (2024).
42. Park, P. et al. PKA drives an increase in AMPA receptor unitary conductance during LTP in the hippocampus. *Nat. Commun.* **12**, 413 (2021).
43. Blackmore, D. G. et al. Low-intensity ultrasound restores long-term potentiation and memory in senescent mice through pleiotropic mechanisms including NMDAR signaling. *Mol. Psychiatry* **26**, 6975–6991 (2021).
44. Shibata, A. C. E. et al. Photoactivatable CaMKII induces synaptic plasticity in single synapses. *Nat. Commun.* **12**, 751 (2021).
45. Li, G., McLaughlin, D. W. & Peskin, C. S. A biochemical description of postsynaptic plasticity—with timescales ranging from milliseconds to seconds. *Proc. Natl. Acad. Sci. USA* **121**, e2311709121 (2024).
46. Gao, Q. et al. PINK1-mediated Drp1S616 phosphorylation modulates synaptic development and plasticity via promoting mitochondrial fission. *Signal Transduct. Target Ther.* **7**, 103 (2022).
47. Ramos-Prats, A. et al. Loss of mGlu5 receptors in somatostatin-expressing neurons alters negative emotional states. *Mol. Psychiatry* **29**, 2774–2786 (2024).
48. Ray, S. et al. Grid-layout and theta-modulation of layer 2 pyramidal neurons in medial entorhinal cortex. *Science* **343**, 891–896 (2014).
49. Kitamura, T. et al. Island cells control temporal association memory. *Science* **343**, 896–901 (2014).
50. Ormond, J. & O'Keefe, J. Hippocampal place cells have goal-oriented vector fields during navigation. *Nature* **607**, 741–746 (2022).
51. Long, X. & Zhang, S. J. A novel somatosensory spatial navigation system outside the hippocampal formation. *Cell Res.* **31**, 649–663 (2021).
52. Qasim, S. E., Fried, I. & Jacobs, J. Phase precession in the human hippocampus and entorhinal cortex. *Cell* **184**, 3242–3255.e10 (2021).
53. Kula, B. et al. D-β-hydroxybutyrate stabilizes hippocampal CA3–CA1 circuit during acute insulin resistance. *PNAS nexus* **3**, pgae196 (2024).
54. Wu PY, Ji L, De Sanctis C, Francesconi A, Inglebert Y, McKinney RA. Loss of synaptopodin impairs mGluR5 and protein synthesis–dependent mGluR-LTD at CA3-CA1 synapses. *PNAS Nexus* **3**, 1371 (2024).
55. Dong, C., Madar, A. D. & Sheffield, M. E. J. Distinct place cell dynamics in CA1 and CA3 encode experience in new environments. *Nat. Commun.* **12**, 2977 (2021).
56. Ohara, S. et al. Hippocampal-medial entorhinal circuit is differently organized along the dorsoventral axis in rodents. *Cell Rep.* **42**, 112001 (2023).
57. Vandrey, B., Armstrong, J., Brown, C. M., Garden, D. L. & Nolan, M. F. Fan cells in lateral entorhinal cortex directly influence medial entorhinal cortex through synaptic connections in layer 1. *eLife* **11**, e83008 (2022).
58. Lopez-Rojas, J., De Solis, C. A., Leroy, F., Kandel, E. R. & Siegelbaum, S. A. A direct lateral entorhinal cortex to hippocampal CA2 circuit conveys social information required for social memory. *Neuron* **110**, 1559–1572.e4 (2022).
59. Caputi, A., Liu, X., Fuchs, E. C., Liu, Y. C. & Monyer, H. Medial entorhinal cortex commissural input regulates the activity of spatially and object-tuned cells contributing to episodic memory. *Neuron* **110**, 3389–3405.e7 (2022).
60. Ben-Simon, Y. et al. A direct excitatory projection from entorhinal layer 6b neurons to the hippocampus contributes to spatial coding and memory. *Nat. Commun.* **13**, 4826 (2022).
61. Zutshi, I. & Buzsáki, G. Hippocampal sharp-wave ripples and their spike assembly content are regulated by the medial entorhinal cortex. *Curr. Biol.* **33**, 3648–3659.e4 (2023).
62. Axelrod, C. J., Gordon, S. P. & Carlson, B. A. Integrating neuroplasticity and evolution. *Curr. Biol.* **33**, R288–R293 (2023).
63. Cao, N. et al. Clinical-grade human umbilical cord-derived mesenchymal stem cells reverse cognitive aging via improving synaptic plasticity and endogenous neurogenesis. *Cell Death Dis.* **8**, e2996–e2996 (2017).
64. Kiritoshi, T. et al. Cells and circuits for amygdala neuroplasticity in the transition to chronic pain. *Cell Rep.* **43**, 114669 (2024).
65. Vestring, S. et al. D-Cycloserine enhances the bidirectional range of NMDAR-dependent hippocampal synaptic plasticity. *Transl. Psychiatry* **14**, 18 (2024).
66. Masella, G. et al. The amygdala NT3-TrkC pathway underlies inter-individual differences in fear extinction and related synaptic plasticity. *Mol. Psychiatry* **29**, 1322–1337 (2024).

67. Weichard, I. et al. Fully-primed slowly-recovering vesicles mediate presynaptic LTP at neocortical neurons. *Proc. Natl. Acad. Sci. USA* **120**, e2305460120 (2023).
68. Boccara, C. N., Nardin, M., Stella, F., O'Neill, J. & Csicsvari, J. The entorhinal cognitive map is attracted to goals. *Science* **363**, 1443–1447 (2019).
69. Wong, Y. T. et al. Artificial fluorescent sensor reveals pre-synaptic NMDA receptors switch cholecystokinin release and LTP in the hippocampus. *J. Neurochem.* **168**, 2621–2639 (2024).

Acknowledgements

This work was supported by Hong Kong Research Grants Council, General Research Fund: 11103220M, 11101521M (GRF, JFH); Hong Kong Research Grants Council, Collaborative Research Fund: C1043-21GF (CRF, JFH); Innovation and Technology Fund: MRP/053/18X, GHP_075_19GD (ITF, JFH); Health and Medical Research Fund: 06172456, 09203656 (HMRF, XC, JFH). All cartoons are created with BioRender.com (https://app.biorender.com/).

Author contributions

J.H. and F.H. designed and conceived this study. F.H. performed the experiments, collected and analyzed data. F.H., S.T.B., and S.H.L. contributed to data analysis and interpretation. F.H. wrote the paper. J.H. finalized the paper.

Competing interests

The authors declare no competing interests.

Additional information

Supplementary information The online version contains supplementary material available at https://doi.org/10.1038/s42003-026-09577-z.

Correspondence and requests for materials should be addressed to Fengwen Huang or Jufang He.

Peer review information *Communications Biology* thanks Yiding Li and the other, anonymous, reviewer(s) for their contribution to the peer review of this work. Primary Handling Editor: Jasmine Pan. A peer review file is available.